Full-Color Waveguide-type Near-Eye Displays with Huygens' Metasurfaces

Weitao Song, Xinan Liang, Qijia Cheng, Parikshit Moitra, Xuewu Xu, Weijia Zhang, Xiaogang Shi, Yuanjin Zheng, Yongtian Wang, Ramón Paniagua-Domínguez*, Arseniy I. Kuznetsov**

Weitao Song, Weijia Zhang, Yongtian Wang
Beijing Engineering Research Center of Mixed Reality and Advanced Display, School of Optics and Photonics, Beijing Institute of Technology, 5 Zhongguancun South Street, Beijing, 100081, China
email: swt@bit.edu.cn

Xinan Liang, Parikshit Moitra, Xuewu Xu, Ramón Paniagua-Domínguez, Arseniy I. Kuznetsov
Institute of Materials Research and Engineering (IMRE), Agency for Science, Technology and Research (A*STAR), 2 Fusionopolis Way, Innovis #08-03, Singapore 138634, Republic of Singapore
National Semiconductor Translation and Innovation Centre (NSTIC), 4 Fusionopolis Way, Kinesis, #09-11, Singapore 138635, Republic of Singapore
email: Ramon_Paniagua@imre.a-star.edu.sg, and
Arseniy_Kuznetsov@imre.a-star.edu.sg

Qijia Cheng, Yuanjin Zheng
School of Electrical and Electronic Engineering, Nanyang Technological University, 50 Nanyang Avenue, 639798 Singapore

Xiaogang Shi
School of Integrated Circuits and Electronics, Beijing Institute of Technology, 5 Zhongguancun South Street, Beijing, 100081, China

Keywords: metasurface, near-eye displays, holography, waveguide, full color

Abstract:

Miniaturized and lightweight see-through near-eye displays are desirable for wearable computing applications. With the recent rapid advances in ultra-thin metasurface optics, the compactness and weight of near-eye displays can be improved without compromising the performance of the real-virtual scene. In this paper, a proof-of-concept solution, using transparent Huygens' metasurface hologram as the display device, is developed to provide full-color images. A virtual image is created by illuminating three 500μm metasurface holograms, spaced 500μm apart, with red, green, and blue light sources, and combining the resulting holographic images in a diffractive waveguide to produce a full-color image in front of the viewer's eyes. Using this method, we experimentally demonstrate a compact and wearable near-eye display with a thin (1.2mm) waveguide in front of the viewer's eyes, creating a virtual image with a large field of view (≥40°) that can be viewed along with the real world within a large eye box (15mm × 10mm). To achieve this, we introduce a new design method exploring the potential of metasurface holograms as an image source for mobile computing in daily life.

1. Introduction

Recently, the emergence of the metaverse has sparked a surge of interest in head-mounted displays (HMD) or near-eye displays (NED), which can provide virtual images in front of the viewer's eye. NEDs, which are also treated as the entrance of the metaverse for human beings [1-3], can be divided into two types. The first type immerses the user in a completely virtual scene generated by computers, often used in virtual reality (VR) applications [4]. To achieve a VR-type NED with a lightweight, large field of view (FOV), large eye box, and high resolution, aspherical plastic optics, Fresnel optics, or holographic optics have been employed to replace traditional spherical glass optics [5-6]. A recent emerging approach utilizes catadioptric optics, so-called pancake lenses [7-8], to realize an ultra-thin form factor. This is the case, e.g. in the recently released Apple Vision Pro [9]. The second type of NED allows the viewers to perceive a mixed-reality world by superimposing virtual information onto real-world scenes, often called optical see-through or augmented reality (AR) NED [10-12]. AR NED holds the potential to be essential in our future daily lives, enhancing how we interact with the world and the information around us. For this, typically, partially reflective structures should be employed to achieve the goal of optical see-through, making it more complicated to design an optical see-through NED than an immersive one. To realize them, freeform surfaces and off-axis refractive and reflective

structures have been developed [13-14]. To obtain a good performance, the optics for these structures should provide a large FOV and exit pupil, which has been proven hard to miniaturize. Among these approaches, the most compact one consists of a projection optics module and a total internal reflection (TIR) waveguide, which can be a geometrical waveguide or a diffractive waveguide [15-16]. The light beam from the image source can be collimated with projection optics, then reflected in the waveguide multiple times, and finally coupled out from the waveguide and projected into the viewer's eye. Pupil duplication techniques can be used to enlarge the beam size, and a large eye box is achieved with small exit-pupil projection optics, which can decrease the size of the eyepiece greatly. As for the image source, different types of devices, such as Liquid Crystal on Silicon (LCOS), digital micromirror devices (DMD), organic light emission diodes (OLED), or mini light emission diodes (mini-LED) have been applied [17-20]. To make the system more compact, the image source and the projection lens should be optimized together. Despite over seventy years of efforts since the 1960s, balancing and optimizing these performance features of displays simultaneously remains a challenge.

Metasurfaces, a new class of ultra-thin planar optical elements consisting of artificially fabricated subwavelength nanostructures, has attracted a lot of interest from both academia and industry, due to its superior modulation capabilities of incident light beam [21]. Indeed, these devices offer unparalleled spatial resolution (with pixels that can be sub-wavelength in nature), while enabling almost full and arbitrary control over the local amplitude, phase, and polarization of the wave. Various mechanisms have been adopted to design metasurfaces, particularly those that modulate the phase, ranging from those using resonances, both plasmonic-based [22] and dielectric-based [23-24], to those using the propagation phase [25], geometric phase (Pancharatnam Berry phase [26]), or topological phase [27]. Thanks to the enormous design degrees of freedom that metasurfaces make accessible, multiple optical functions can be integrated into a single planar device. Also, compared to traditional optical components, metasurface components could miniaturize the system and be fabricated at scale using CMOS-like processes. Due to these attractive properties, various component and system-level demonstrations have been reported, including lensing [26, 28-35], holograms [36-42], beam bending and steering devices [43-48], multifunctional devices [49], vortex beam generation [50], and many others.

As mentioned above, within the context of VR and AR, a lightweight and compact display device with high performance is required. Due to its strong and flexible light-modulating capabilities, metasurfaces can also be introduced in NED to obtain a promising solution to

improve performance. A typical NED system consists of an optical magnification subsystem (eyepiece) and an image source. During the usage, virtual images can be generated and loaded on the display device and then imaged at a relatively far distance in front of the viewer's eyes by the eyepiece. The eyepiece is normally a single-component or multi-component lens system or a combination of a projection lens and a waveguide. In this context, metasurface-based components have been exploited to realize or improve some of the functions of the eyepiece in a compact form, e.g. incorporating an element with a large FOV [51], reducing the size by employing a full-color achromatic metasurface [52-53], integrating a metasurface along with freeform surfaces [54], designing a polarization sensitive in-coupler [55] or introducing metasurface gratings with high diffraction efficiency [56]. Moreover, as a metasurface can provide a virtual image with a large diffraction angle and high diffraction efficiency, it can act, along with an illumination beam, as an image source in NED systems, which can also be explored as an ideal candidate for holographic displays. When a metasurface-based hologram is used as an image source, the display system can be compact and lightweight, with simple reconstruction optics. Indeed, various metasurface holograms have been demonstrated for display applications in recent years [36-42]. While most of these demonstrations are static, various material systems (phase change materials, semiconductors, transparent conductive oxides, liquid crystals, etc.) and stimuli (thermal, electrical, and optical) are being explored to realize tunable metasurfaces [24] that hold the potential to be used in displays as dynamic SLMs to generate dynamic images or encode computer-generated holograms (CGH). Therefore, the potential ability of metasurfaces, and in particular metasurface holograms, to be used as an image source for different display applications should be explored to provide useful references for the design of future displays. The simplest approach is using a metasurface hologram as an image source for projection-type display, and indeed both single and multiple colors devices of this kind have been demonstrated [38-39]. Recently, single-color metasurface holograms have also been used in NED systems as the image source [37, 57]. For full-color NED systems that can be viewed with the naked eye, however, a holistic design that considers the whole system is crucial, tackling simultaneously many issues that might arise in this type of system, such as color fusion, compactness, image quality, etc.

This work demonstrates that three metasurface holograms and small light sources may further miniaturize NED systems with simple optics. As mentioned above, images with three color channels can be projected into waveguides and full-color virtual images can be generated by merging the three channels in the waveguides. Thanks to the high phase mapping resolution of

metasurfaces, this type of image source, together with compact lasers, can provide a high-resolution virtual image in a small active display area. Due to the exit pupil expansion feature of diffractive waveguides, a system with a small-size metasurface hologram can achieve an optical see-through image with a large eye box and FOV. Furthermore, virtual images from different projection channels can be merged into a full-color image. Our approach also allows for the metasurface holograms for RGB channels to be designed and fabricated separately, which could be more convenient for bringing dynamic metasurface devices (typically monochromatic) to the future display market. Based on these considerations, we design and experimentally demonstrate a compact full-color waveguide-type NED system using a transmissive dielectric Huygens' metasurface hologram as the image source, able to provide full-color images with a large eye box and a large FOV that can be directly viewed along with the real scene.

2. Results

2.1. Full-color waveguide-type near-eye displays with metasurface holograms.

As illustrated in **Figure 1**, the display device consists of three metasurface holograms fabricated on a single glass substrate and works with illumination sources (typically three, with three different colors) to project the desired image. Note that each metasurface hologram is wavelength-sensitive and should be designed for the corresponding operation wavelength. An optional color filter can also be used between the illumination sources and the metasurfaces. Since the three small-sized holograms are spatially separated, the virtual images for different color channels may not merge perfectly, resulting in a smaller aperture. In a diffractive waveguide, the beams for different color channels are replicated parallelly by each total internal reflection. Thus, while the images and colors may not overlap perfectly in space, the designed pattern of the waveguide ensures that images for all three colors enter the viewer's eye within the eye box.

Additionally, since the diameter of the human pupil is at least 2mm, the aperture of the projection optics should be enlarged to produce a large eye box. The aperture of metasurface holograms is normally in the scale of several hundred micrometer which is much smaller than that of commercial image sources. Thus, the image aperture should be enlarged with the help of the pupil duplication function of the waveguide. Real images far away from the hologram (which can be treated at an infinite distance) can be reconstructed directly by the metasurface

when a collimated laser beam illuminates it. Then, after replicating multiple times the beams, they are reflected out of the waveguide and to the viewer's eye by the out-coupler on the waveguide surface with a large eye box. In this design, we can observe the real world through the waveguide, and the holographic image can be superimposed with the real scene.

2.2. Design and performance of the metasurface holograms

Following the design principle described in the previous section, a waveguide-type wearable NED was designed and fabricated. **Figure 2a** shows the system layout. It consists of laser sources, optional color filters, diffractive type waveguides, and metasurface holograms (acting as the image sources). Here, each laser source illuminates the corresponding metasurface holograms, and the holographic images are then projected onto the in-coupler of the waveguide. The axis of laser illumination and the display device is tilted by 25° from the waveguide normal to prevent the possible zeroth order diffraction (direct transmission of incident light) from entering the field of view. The images for the three colors can merge and the eye box can be expanded when they pass through the waveguide. Finally, the full-color image is projected into the viewer's eye via out-couplers, allowing it to be seen along with the real-world scene.

Two groups of diffractive elements were designed for the green-blue channel and red channel of the waveguide respectively, due to the wavelength sensitivity of the diffractive structure, and bonded with each other with a protective glass. A three-grating structure was adopted for the waveguide design, consisting of in-coupling grating, turning grating, and out-coupling grating, all embedded into the glass waveguide. The waveguide parameters, layout, and images are shown in **Figures S1-S6** in the supplementary information. The in-coupling grating couples the projection light beam, in which the holographic image information is embedded, into the substrate, which then guides it towards the turning grating, which directs light toward the outcoupling grating. The pupil is duplicated and enlarged vertically by the turning grating and is expanded horizontally by the outcoupling grating before the light beam reaches the viewer's eye. The parameter selection of these gratings for different wavelengths has been discussed in previous works [57-58] and is schematically shown in **Figure S2**. In the diffractive waveguide, the beams for different color channels are replicated parallelly at each reflection. To obtain a large eye box and an image with full color, the design parameters, including the refractive index, thickness, and phase distribution of each grating, were analyzed and optimized using commercial optical design software (Synopsys Lighttools), as shown in **Figure S7**. As the eye pupil cannot be less than 2mm, the distance between adjunct beams emitting from the

waveguide should not be larger than 2mm. Based on the optimized parameters, images projected from each metasurface holograms with an aperture of 0.5mm can be viewed by the viewer's eye within an eye box of 15mm × 10mm and with a field of view of 40 degrees. **Figure S8** also gives the diffraction efficiency of the waveguide as a function of wavelength, which can reach the average level of commercial products.

For the color image demonstration, three 500μm × 500μm metasurface holograms based on TiO2 nanoantennas are used as the red, green, and blue (RGB) channels of the virtual images. To achieve the full 0-2π phase control in transmission with reduced fabrication aspect ratios, we choose to use Huygens'-type metasurfaces. They enable high transmission and 2π phase modulation simultaneously by carefully tuning the spectral positions of the electric dipole (ED) and magnetic dipole (MD) resonances excited in the nanoantennas. When the induced dipole moments associated with ED and MD have the same amplitude and phase, the backward scattering from the nanoantennas is suppressed, which means the Huygens condition is met. This results in a near-unity transmission through the metasurface with a 2π phase modulation around the resonant wavelength [45, 60, 61]. For our operation wavelengths of 662nm (red, R), 532nm (green, G), and 473nm (blue, B) the following nanoantenna heights and lattice pitches have been selected through design optimization: hR = 172nm and PR = 420nm for red, hG = 125nm and PG = 340nm for green, and hB = 113nm and PB = 305nm for blue. The simulated performance of the designed, disk-shaped TiO2 Huygens metasurfaces is presented in **Figure 2**. The nanodisks are arranged in a square lattice and placed on a SiO2 substrate. For each specific wavelength, the thickness and diameters of the disks are optimized using a commercial finite-difference time-domain (FDTD) simulation software (ANSYS Lumerical) to achieve the Huygens condition at the corresponding wavelength, and a periodical boundary condition is used for the simulation. The parameters to accomplish the Huygens' condition are summarized in Table S1, and the transmission and phase modulation spectra of the nanoantenna designed for RGB channels are shown in **Figure 2c-e**. From the transmission spectrum, we can see the merge of the corresponding ED and MD dips in the spectrum, and the transmission is larger than 0.9 for green and blue, and 0.85 for red, at the same time there is a 2π phase shift around that operational wavelengths. This is a typical feature of the Huygens metasurface[45]. The electric and magnetic field distribution in the antenna designed for wavelength 532nm at Huygens condition is shown in supplementary materials. After obtaining the optimized diameter of the nanodisk, they are varied around the optimized value, as shown in **Figure 2f-h**, to induce the phase modulation of ~2π. Over the 2π range, 8 phase levels corresponding to the

phase modulations step of π/4 are chosen to digitalize the holograms. With the change in the diameter of the nanodisk, the transmission drops due to the partial detuning of the overlap of the ED and MD dipole. It is slightly off the exact Huygens condition. It is worth noting that the phase modulation for each wavelength falls in a limited spectrum range, as shown in **Figure 2i**, and there is a clear separation between red, green, and blue colors. To check the performance of the designed metasurface, nanodisks with different diameters corresponding to the 8 equally-spaced phase levels covering the 2π phase range were arranged in a supercell to form a blazed phase grating. The diffraction efficiencies of these blazed gratings for different colors were numerically calculated and summarized in Table S2 and shown in **Figure 2j**.

To compute the point-cloud-based phase-type holograms a coherent ray tracing approach [62] was used. The coherent ray tracing algorithm is selected in this report, as it can provide high-quality reconstruction and can support large-angle displays. As mentioned above, the projection plane of the generated holographic image can be infinitely far away. Here a large distance of around 10cm is used, which, compared to the 500μm × 500μm hologram size, can be treated as infinite. A point cloud image comprising three sets of letters "A*STAR", "BIT" and "NTU" surround a symbol of a star, and two flower symbols are selected to verify the proposed display method, which contains both separate colors and merged color image parts (**Figure 2b**). Each generated point can be treated as a point-light source and is propagated to the hologram plane. The complex field distributions at the hologram plane from point sources are summed up and form a complex hologram, in which all the information about the object is encoded. Due to the complexity of independently manipulating amplitude and phase, the amplitude information in the complex hologram is discarded and the amplitude is set to unity, thus forming a pure phase-type hologram. Finally, the obtained phase profile is mapped with the designed nanoantennas forming the final metasurface hologram.

To achieve the different required heights the three metasurface holograms (R, G and B) were fabricated on one glass plate with a relatively large separation distance of 0.5mm via a specially developed staircase lithography process (see more details in Methods). In brief, the three metaholograms are first patterned and transferred into a 180nm thick TiO2 film using electron beam lithography and etching. The red metahologram is then masked with a protective layer, and the metaholograms patterns for green and blue channels are further etched down to the desired thicknesses using an ICP dry etching process. Then, the protective layer for the red metahologram is removed by heating the sample in a Piranha bath. A characteristic scanning electron microscope (SEM) image of one of the holograms is shown in **Figure S10**. Before

assembling the fabricated holograms as image sources for the NED, their peak diffraction efficiencies are measured to be 8.01%, 14.05%, and 15.75% at wavelengths of 658nm, 510nm, and 468nm, respectively (**Figure 2k**). Compared to the simulated diffraction efficiencies (30.2%, 36.0%, and 32.5% for red, green, and blue) shown in **Figure 2j** for 8-phase level blazed gratings, the peak positions matched well with the designed wavelengths for red (662nm) and blue (473nm) channels. A slightly larger deviation is observed for the green channel (510nm vs 532nm), which can be attributed to fabrication imperfections. The moderate diffraction efficiencies of the Huygens' metaholograms can be explained by inter-particle coupling in the arrays, which causes a deviation of the experimental phase values from the simulated ones (since the simulations are done for the uniform nanoantenna arrays and the measurements are for the non-uniform hologram patterns).

2.3 Performance of the near-eye displays using the metasurface holograms

A prototype of a waveguide-type near-eye display was set up with the fabricated metasurface holograms based on the design described in the previous sections. **Figure S11** shows a photo of the assembled setup. A white screen was used to display the projection image, and a single-lens reflex camera was used to capture the image. **Figure 3** shows the projection performance of the metasurface hologram, including the results of any two of the R, G, and B channels. Images with full color can be seen on the screen, e. g. white color can be obtained by merging all three channels. It should be noted that the merged image has a slight displacement due to the separate design structure for the three holograms. Off-axis illumination methods, as demonstrated in previous studies [63-64] can be used, which can reduce the crosstalk and displacement among different wavelengths by obliquely projecting laser beams onto the metasurface. In our proposed near-eye display method, the illumination method can be achieved by an easy way, and the displacement can be solved within the waveguide due to the pupil duplication properties.

To make the system easy to wear, a spectacle frame is designed and manufactured by 3D printing to hold the laser source, the waveguide, the mirrors, the metasurface holograms, and the optical attenuator (optional), which is shown in **Figure S12**. Here, a button cell or other portable power devices can be used to power the laser source, and an optical attenuator is included to reduce the intensity of the light to protect the eyes. In the future, when dynamically tunable metasurface devices are developed, a compact full-color AR near-eye display with a better design can be achieved using the proposed method. **Figure 4** shows the augmented

information displayed by the system and the real world, as captured by the single-lens reflex camera. As can be seen, the reconstruction through the waveguide system is not as good as the hologram reconstruction in the free space shown before. This is mainly due to the stray light within the waveguide and the speckle noise caused by using a laser as the illumination source. The stray light can be further reduced by optimizing the structure of the waveguide, and the speckle noise can be removed using different approaches such as random phase averaging and/or camera-in-the-loop neural network algorithms [11]. All these techniques and the possibility of using dynamically tunable metasurface devices can be introduced to improve image quality in the future. We note that the transmissive character of the metasurfaces or their physical separation is not an essential feature and slightly modified designs could be adapted for reflective metadevices or time-sequential color rendering.

3. Conclusion

In summary, we have proposed and demonstrated a proof-of-concept solution for a full-color, lightweight, and compact NED system including three separated transmissive metasurface holograms as the image sources. These spatially separated metaholograms can be fabricated on the same substrate with a so-called staircase metasurface fabrication method. A diffractive waveguide is then utilized to enlarge the projection aperture of the metasurface holograms and merge them into a full-color virtual image that can be observed directly by the viewer's eye within a large eye box. The developed method can ultimately miniaturize the current NED systems, promoting the development of mobile AR on smartphones and wearable AR products displays in the consumer electronics market in the future, finding widespread applications in our daily lives.

4. Methods

Metasurface Hologram Fabrication Process: Figure S13 shows the fabrication process of metasurface hologram. First, titanium dioxide (TiO_2) film of 180 nm in thickness is deposited using a dual beam ion-assisted deposition system (Oxford Optofab 3000) on a 2.5 cm × 2.5 cm quartz substrate with 0.7 mm thickness. The complex refractive index of TiO_2 is measured using spectroscopic ellipsometry (Woollam) and is used to determine the precise film thickness using the Filmetrics tool. After that, a 30 nm Cr thin film is evaporated on top of the TiO_2 layer using an electron beam evaporator (Angstrom), followed by spin coating and soft baking of negative tone electron beam resist Hydrogen Silsesquioxane (HSQ). Three arrays of 500 μm × 500 μm

dimensions (corresponding to red, green, and blue color hologram channels) separated by 500 μm gaps are patterned using electron beam lithography (Elionix ELS-7000), followed by the development of patterns in a salty developer (NaOH/ NaCl). The HSQ patterns are used as masks to etch the chromium (Cr) layer underneath using an Oxford Plasma Etch, which is an inductively coupled plasma (ICP) reactive ion etching (RIE) tool, using Cl_2 and O_2 gases. The etched Cr disk patterns are then used as masks to etch the underlying TiO_2 using CHF_3 gas in the SPTS (KLA) tool (ICP RIE). Cr patterns are then removed using wet chemical etching using commercial Cr etchant. All three metasurface arrays now consist of nanodisks with 180 nm thickness. To reduce the thickness of TiO2 nano disks corresponding to G and B metasurfaces, the R metasurface is masked by spin coating the substrate with positive S1811 photoresist (thickness ~1.5 μm), followed by exposing the resist in a mask aligner (EVG 62008 Infinity) with 405nm light through a photomask which blocks the R metasurface array with a square of 525 μm × 525 μm and let the rest of the resist expose. After developing the pattern, the substrate is put through another ICP RIE process to reduce the height of G and B arrays, while the R array stays unaltered under the resist mask. After the height reduction, the resist mask from R is removed by heating the substrate in a Piranha solution bath.

Diffractive Waveguide Fabrication Process: The full-color waveguide consists of one protective glass (SCHOTT BK7) and two pieces of diffractive waveguides with different parameters. Both waveguides are made of glass (Hoya TAFD25, refractive index of 1.9) with a thickness of 0.35 mm. The gratings are made from a photoresist (Inkron IOC-133, refractive index of 1.9) using nanoimprinting (Obducat Eitre ™ 8 NanoImprinter). The imprint mold for the nanoimprinting process is fabricated by Electron Beam Lithography (JEOL JBX-9500FS) with dry-etching technology (Lam Research 2300 kiyo 45). **Figure S14** shows the fabrication process of the nanoimprint mold. A UV gel is used to integrate the waveguide and an air gap of 0.1mm is set between the waveguides, which guarantees the total internal reflection.

Characterization and measurements: The size and morphology of the metasurfaces are characterized by a scanning electron microscope (Hitachi SU8220). To measure the diffractive efficiency of the metasurface hologram, a supercontinuum source (SuperK EXTREME, NKT Photonics) along with a tunable filter (SuperK SELECT, NKT Photonics) is used as the light source. The intensities of the incident light and the generated images are measured with an optical power meter (Thorlabs PM320E Model Console + S120C Detector). The display performance is recorded by a single-lens reflex camera (SONY α7 IV, with a standard lens of FE35mm F1.8). To meet the Huygens' metasurface operation requirements, the laser beam is

collimated and incident normally to the metasurfaces. The beam size is controlled with a pinhole (diameter of 500μm) to cover the hologram (500 μm × 500 μm) appropriately. The incident light intensity is measured after the pinhole and before the hologram. The intensity of the reconstructed image is measured with the help of a condenser lens to guarantee the diffracted light is correctly collected by the photodetector of the power meter. The diffraction efficiency is calculated as the ratio of the first-order diffraction intensity to the incident light intensity.

Acknowledgments

Funding: This work was supported by the National Natural Science Foundation of China (62475013,62332003), A*STAR RIE2020 AME Programmatic Funding (A18A7b0058), and the National Research Foundation of Singapore under Grant No. NRF-NRFI2017-01.
Conflict of interest: The authors declare no conflict of interest.
Author Contributions: W.S. and X.L. contributed equally to this work. W.S., X.L., Q.C, Y.Z., R.P.D, and A.I.K. conceived the idea and designed the experiments. W.S, X.L, X. S. and Y.W designed the optical system, calculated the hologram, and characterized the display performance. X.X and P.M. performed the design, optimization, fabrication, and characterization of the metasurface. W.S., X.L., Q.C., Y.Z., R.P.D., and A.I.K. co-wrote the paper. All authors contributed to the analysis and discussions of the results.
Data and materials availability: All data needed to evaluate the conclusions in the paper are present in the paper and/or the Supplementary Materials. Additional data related to this paper may be requested from the authors.

Received: ((will be filled in by the editorial staff))
Revised: ((will be filled in by the editorial staff))
Published online: ((will be filled in by the editorial staff))

References

[1] T. Zhan, K. Yin, J. Xiong, Z. He, S.-T. Wu, *iScience* **2020**, 23, 101397.

[2] C. Chang, K. Bang, G. Wetzstein, B. Lee, L. Gao, *Optica* **2020**, 7, 1563-1578.

[3] J. Xiong, E.-L. Hsiang, Z. He, T. Zhan, S.-T. Wu, Light: Science & Applications **2021**, 10, 216.

[4] O. Cakmakci, J. Rolland, *Journal of Display Technology* **2006**, 2, 199-216.

[5] D. Cheng, Q. Wang, Y. Liu, H. Chen, D. Ni, X. Wang, C. Yao, Q. Hou, W. Hou, G. Luo, Y. Wang, *Light: Advanced Manufacturing* **2021**, 2, 350-369.

[6] J. Kim, S. University, U. Manu Gopakumar, S. Choi, Y. Peng, G. Wetzstein, M. Gopakumar, W. Lopes, *In ACM SIGGRAPH 2022 Conference Proceedings* **2022**, 1-9.

[7] J. A. La Russa, *US Patent* **1976**, 3, 940, 203.

[8] O. Cakmakci, Y. Qin, P. Bosel, G. Wetzstein, *Optics Express* **2021**, 29, 35206-35215.

[9] "Apple Vision Pro," can be found under https://www.apple.com/apple-vision-pro/.

[10] Y. Itoh, T. Langlotz, J. Sutton, A. Plopski, *ACM Computing Surveys* **2022**, 54, 1-36.

[11] H. Hua, *Proceedings of the IEEE* **2017**, 105, 805-824.

[12] Y. Li, X. Huang, S. Liu, H. Liang, Y. Ling, Y. Su, Department of Electronic Engineering, Shanghai Jiao Tong University, Shanghai 200240, China, State Key Laboratory of Optoelectronic Materials and Technologies, School of Physics, Sun Yat-Sen University, Guangzhou 510275, China, *Opto-electronic science* **2023**, 2, 230025.

[13] D. Cheng, J. Duan, H. Chen, H. Wang, D. Li, Q. Wang, Q. Hou, T. Yang, W. Hou, D. Wang, X. Chi, B. Jiang, Y. Wang, *Photonics research* **2022**, 10, 21-32.

[14] J. Jeong, C.-K. Lee, B. Lee, S. Lee, S. Moon, G. Sung, H.-S. Lee, B. Lee, *IEEE Photonics Technology Letters* **2020**, 32, 991-994.

[15] A. Maimone, A. Georgiou, J. S. Kollin, *ACM Transactions on Graphics* **2017**, 36, 1-16.

[16] D. Cheng, Y. Wang, C. Xu, W. Song, G. Jin, *Optics Express* **2014**, 22, 20705-20719.

[17] S. Lee, Y. Jo, D. Yoo, J. Cho, D. Lee, B. Lee, *Nature Communications* **2019**, 10, 2497.

[18] M. Gopakumar, G.-Y. Lee, S. Choi, B. Chao, Y. Peng, J. Kim, G. Wetzstein, *Nature* **2024**, 629, 791-797.

[19] Y. Peng, S. Choi, J. Kim, G. Wetzstein, *Science Advances* **2021**, 7, eabg5040.

[20] K. Aksit, P. Chakravarthula, K. Rathinavel, Y. Jeong, R. Albert, H. Fuchs, D. Luebke, *IEEE Trans. Visual. Comput. Graphics* **2019**, 25, 1928-1939.

[21] A. I. Kuznetsov, M. L. Brongersma, J. Yao, M. K. Chen, U. Levy, D. P. Tsai, N. I. Zheludev, A. Faraon, A. Arbabi, N. Yu, D. Chanda, K. B. Crozier, A. V. Kildishev, H. Wang, J. K. W. Yang, J. G. Valentine, P. Genevet, J. A. Fan, O. D. Miller, A. Majumdar, J. E. Fröch, D. Brady, F. Heide, A. Veeraraghavan, N. Engheta, A. Alù, A. Polman, H. A. Atwater, P. Thureja, R. Paniagua-Dominguez, S. T. Ha, A. I. Barreda, J. A. Schuller, I. Staude, G. Grinblat, Y. Kivshar, S. Peana, S. F. Yelin, A. Senichev, V. M. Shalaev, S. Saha, A. Boltasseva, J. Rho, D. K. Oh, J. Kim, J. Park, R. Devlin, R. A. Pala, *ACS Photonics* **2024**, 11, 816-865.

[22] N. Yu, F. Capasso, *Nature Materials* **2014**, 13, 139-150.

[23] A. I. Kuznetsov, A. E. Miroshnichenko, M. L. Brongersma, Y. S. Kivshar, B. Luk'yanchuk, *Science* **2016**, 354.

[24] R. Paniagua-Domínguez, S. T. Ha, A. I. Kuznetsov, *Proceedings of the IEEE* **2020**, 108, 749-771.

[25] C. Zhang, S. Divitt, Q. Fan, W. Zhu, A. Agrawal, Y. Lu, T. Xu, H. J. Lezec, *Light: Science & Applications* **2020**, 9, 55.

[26] M. Khorasaninejad, W. T. Chen, R. C. Devlin, J. Oh, A. Y. Zhu, F. Capasso, *Science* **2016**, 352, 1190-1194.

[27] Q. Song, M. Odeh, J. Zúñiga-Pérez, B. Kanté, P. Genevet, *Science* **2021**, 373, 1133-1137.

[28] X. Ni, S. Ishii, A. V. Kildishev, V. M. Shalaev, *Light: Science & Applications* **2013**, 2, e72.

[29] R. Paniagua-Domínguez, Y. F. Yu, E. Khaidarov, S. Choi, V. Leong, R. M. Bakker, X. Liang, Y. H. Fu, V. Valuckas, L. A. Krivitsky, A. I. Kuznetsov, *Nano letters* **2017**, 18, 2124-2132.

[30] S. Wang, P. C. Wu, V.-C. Su, Y.-C. Lai, M.-K. Chen, H. Y. Kuo, B. H. Chen, Y. H. Chen, T.-T. Huang, J.-H. Wang, R.-M. Lin, C.-H. Kuan, T. Li, Z. Wang, S. Zhu, D. P. Tsai, *Nature Nanotechnology* **2018**, 13, 227-232.

[31] J.-S. Park, S. Zhang, A. She, W. T. Chen, P. Lin, K. M. A. Yousef, J.-X. Cheng, F. Capasso, *Nano Letters* **2019**, 19, 8673-8682.

[32] P. Lalanne, P. Chavel, *Laser & Photonics Reviews* **2017**, 11, 1600295.

[33] A. Arbabi, Y. Horie, A. J. Ball, M. Bagheri, A. Faraon, *Nature Communications* **2015**, 6, 7069.

[34] D. Lin, P. Fan, E. Hasman, M. L. Brongersma, *Science* **2014**, 345, 298 -302.

[35] X. Zhang, Q. Chen, D. Tang, K. Liu, H. Zhang, L. Shi, M. He, Y. Guo, S. Xiao, Opto-Electronic Advances 2024, 7, 230126.

[36] Q. Jiang, G. Jin, L. Cao, Adv. *Advances in Optics and Photonics* **2019**, 11, 518-576.

[37] W. Song, X. Liang, S. Li, D. Li, R. Paniagua‐Domínguez, K. H. Lai, Q. Lin, Y. Zheng, A. I. Kuznetsov, *Laser & photonics reviews* **2021**, 15, 2000538.

[38] G. Zheng, H. Mühlenbernd, M. Kenney, G. Li, T. Zentgraf, S. Zhang, *Nature nanotechnology* **2015**, 10 4, 308-312.

[39] Y. Hu, L. Li, Y. Wang, M. Meng, L. Jin, X. Luo, Y. Chen, X. Li, S. Xiao, H. Wang, Y. Luo, C.-W. Qiu, H. Duan, *Nano letters* **2020**, 20, 994-1002.

[40] W. Zhao, H. Jiang, B. Liu, J. Song, Y. Jiang, C. Tang, J. Li, *Scientific Reports* **2016**, 6, 30613.

[41] L. Wang, S. S. Kruk, H. Tang, T. Li, I. I. Kravchenko, D. N. Neshev, Y. S. Kivshar, *Optica* **2016**, 3, 1504.

[42] S. Cao, Z. Chen, R. Zhang, C. Tang, Z. Chen, R. Nie, F. Zhao, S. Huang, Z. Song, Journal of Physics D: Applied Physics Letter 2024, 125, 041703.

[43] M. I. Shalaev, J. Sun, A. Tsukernik, A. Pandey, K. I. Nikolskiy, N. M. Litchinitser, *Nano letters* **2015**, 15 9, 6261-6266.

[44] J. Xu, M. Cua, E. H. Zhou, Y. Horie, A. Faraon, C. Yang, *Optics Letters* **2018**, 43, 5255 -5258.

[45] Y. F. Yu, A. Y. Zhu, R. Paniagua‐Domínguez, Y. H. Fu, B. Luk'yanchuk, A. I. Kuznetsov, *Laser & Photonics Reviews* **2015**, 9, 412 -418.

[46] E. Khaidarov, H. Hao, R. Paniagua‐Domínguez, Y. F. Yu, Y. H. Fu, V. Valuckas, S. L. K. Yap, Y. T. Toh, J. S. K. Ng, A. I. Kuznetsov, *Nano letters* **2017**, 17, 6267 -6272.

[47] S.-Q. Li, X. Xu, R. Maruthiyodan Veetil, V. Valuckas, R. Paniagua-Domínguez, A. I. Kuznetsov, *Science* **2019**, 364, 1087-1090.

[48] A. M. Shaltout, K. G. Lagoudakis, J. Van De Groep, S. J. Kim, J. Vučković, V. M. Shalaev, M. L. Brongersma, *Science* **2019**, 365, 374-377.

[49] H. Kwon, E. Arbabi, S. M. Kamali, M. Faraji-Dana, A. Faraon, *Nature Photonics* **2019**, 14, 109-114.

[50] Y. Yang, W. Wang, P. Moitra, I. I. Kravchenko, D. P. Briggs, J. G. Valentine, *Nano letters* **2014**, 14 3, 1394-1399.

[51] G.-Y. Lee, J.-Y. Hong, S. Hwang, S. Moon, H. Kang, S. Jeon, H. Kim, J.-H. Jeong, B. Lee, *Nature Communications* **2018**, 9, 4562.

[52] Z. Li, P. Lin, Y.-W. Huang, J.-S. Park, W. T. Chen, Z. Shi, C. Qiu, J.-X. Cheng, F. Capasso, *Science Advances* **2021**, 7.

[53] Z. Li, R. Pestourie, J.-S. Park, Y.-W. Huang, S. G. Johnson, F. Capasso, *Nature Communications* **2021**, 13.

[54] D. K. Nikolov, A. Bauer, F. Cheng, H. Kato, A. N. Vamivakas, J. P. Rolland, *Science Advances* **2021**, 7, eabe5112.

[55] Z. Shi, W. T. Chen, F. Capasso, *Proc. SPIE* **2018**, 10676, 1067615.

[56] W.-Q. Chen, D.-S. Zhang, S.-Y. Long, Z.-Z. Liu, J.-J. Xiao, *Applied Optics* **2021**, 60, 3947.

[57] W. Song, X. Liang, S. Li, P. Moitra, X. Xu, E. Lassalle, Y. Zheng, Y. Wang, R. Paniagua‐Domínguez, A. I. Kuznetsov, *Advanced Optical Materials* **2023**, 11, 2202348.

[58] P. Genevet, F. Capasso, F. Aieta, M. Khorasaninejad, R. Devlin, *Optica* **2017**, 4, 139-152.

[59] D. Kong, Z. Zhao, X. Shi, X. Li, B. Wang, Z. Xue, S. Li, *Optics express* **2021**, 29, 36720 -36733.

[60] M. Decker, I. Staude, M. Falkner, J. Dominguez, D. N. Neshev, I. Brener, T. Pertsch, Y. S. Kivshar, *Advanced Optical Materials* **2015**, 3, 813-820.

[61] X. Liang, Y. Yu,; X. Xu, Yuan Hsing Fu, Vytautas Valuckas, R. Paniagua-Dominguez, A. I. Kuznetsov, *Applied optics* **2021**, 61, B164 -B170.

[62] Y. Pan, X. Xu, S. Solanki, X. Liang, R. B. A. Tanjung, C. Tan, T. C. Chong, *Optics express* **2009**, 17, 18543.

[63] X. Li, L. Chen, Y. Li, X. Zhang, M. Pu, Z. Zhao, X. Ma, Y. Wang, M. Hong, X. Luo, Science Advances **2016**, 2, 1601102.

[64] X. Zhang, M. Pu, Y. Guo, J. Jin, X. Li, X. Ma, J. Luo, C. Wang, X. Luo, Advanced Functional Materials **2019**, 29, 1809145.

Figures and Captions

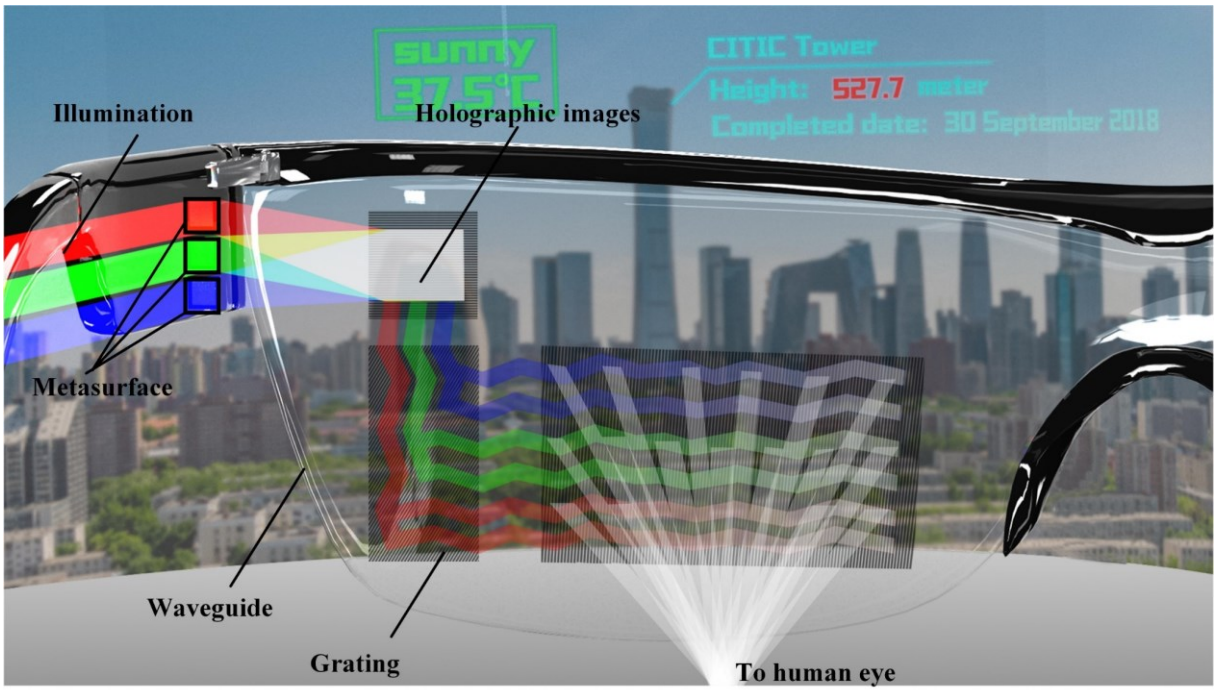

Figure. 1. General illustration of a full-color waveguide-type near-eye display with Huygens' metasurfaces.

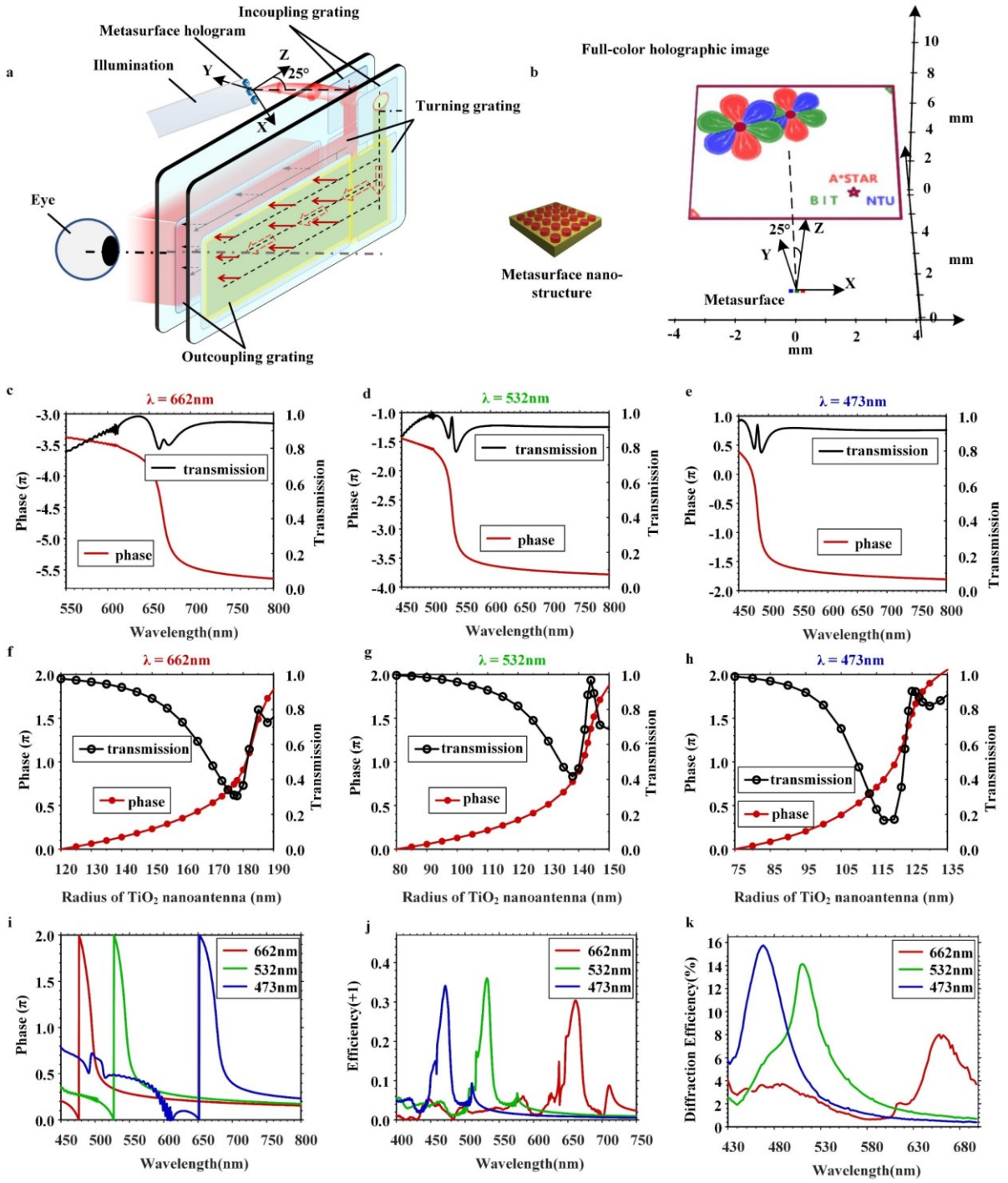

Figure 2. System schematic and design of the metasurface hologram. (a) Illustration of the setup of an optical see-through full-color near-eye display system using transmissive metasurface holograms. **(b)** Spatial position of the reconstructed color images with respect to the metasurface holograms. **(c-e)** Simulated transmission spectra and phase modulation for uniform TiO_2 nanoantenna arrays optimized to achieve Huygens' Condition at R, G, and B wavelengths respectively (see the array parameters in Table S1). **(f-h)**. Simulated $0 \sim 2\pi$ phase modulation together with the transmission spectra from uniform TiO_2 nanoantenna arrays with varied nanoantenna radius around the Huygens' condition at **(f)** R, **(g)** G, and **(h)** B wavelengths.

(i) phase modulation at RGB wavelengths **(j)** Simulated beam deflection efficiency by 8-phase level blazed metasurface grating at RGB wavelengths. **(k)** Measured diffraction efficiencies for the generated images from RGB holograms as a function of the wavelength (normalized to the incident light)

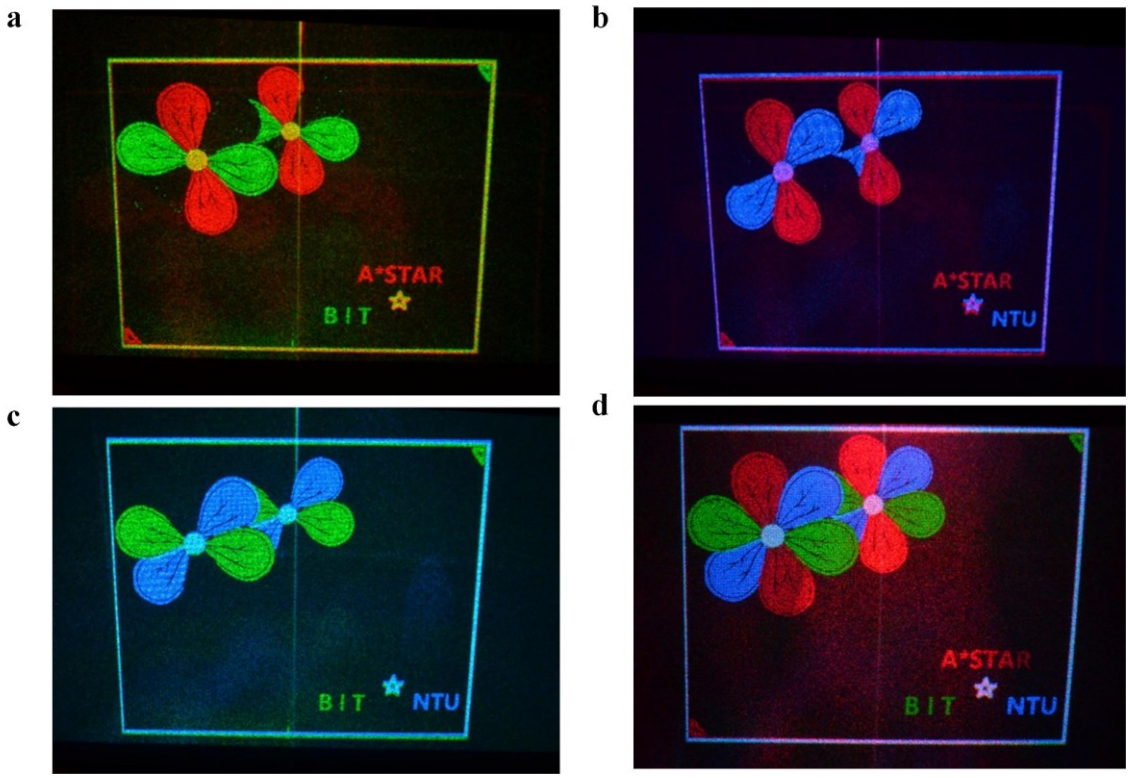

Figure 3. Projection images using the designed metasurface holograms for two channels of **(a)** red & green, **(b)** red & blue, and **(c)** green & blue, and **(d)** all three red, green & blue channels together, are projected on the white screen and captured by the single lens reflex camera.

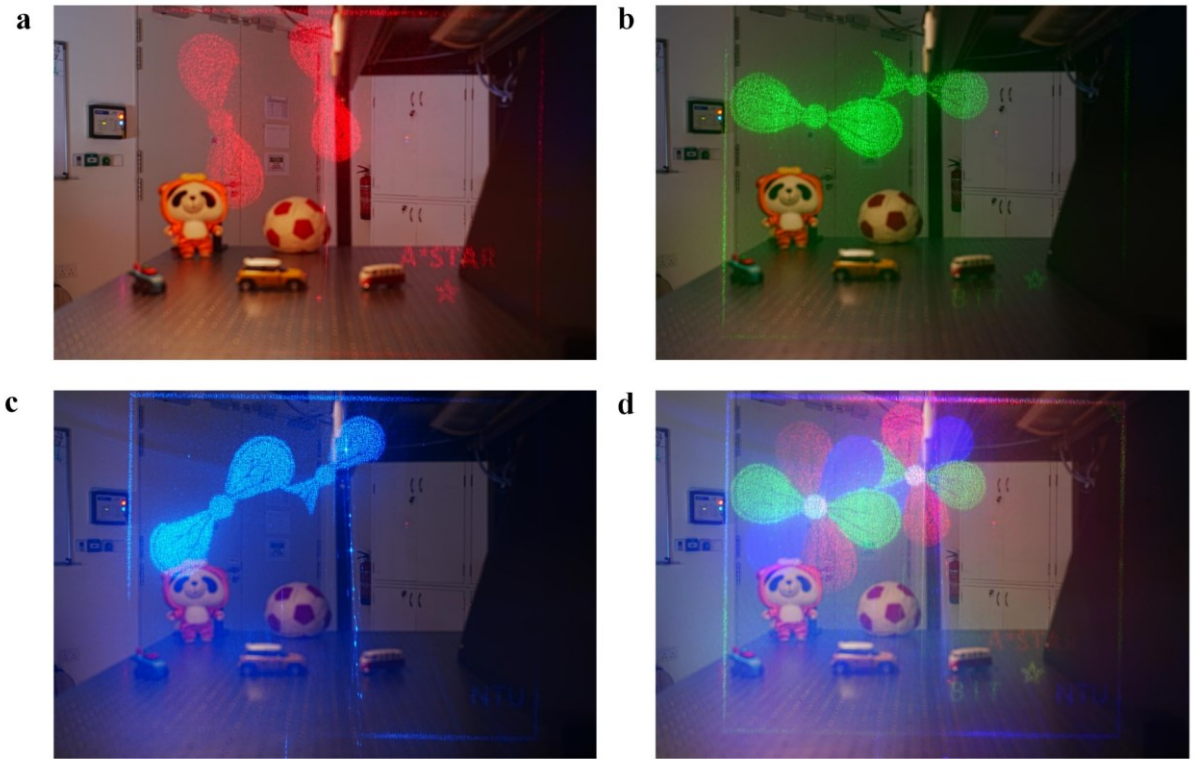

Figure 4. Optical see-through near-eye display using the designed metasurface holograms. **(a-c)** generated images for a single channel of **(a)** red, **(b)** green, and **(c)** blue, captured by a single-lens reflex camera along with the real-world scene. **(d)** Augmented full-color information is displayed by the system along with the real-world scene.

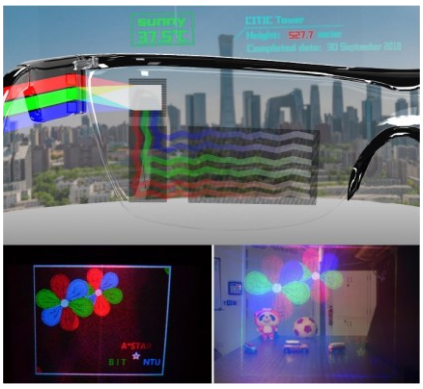

ToC figure ((Please choose one size: 55 mm broad × 50 mm high **or** 110 mm broad × 20 mm high. Please do not use any other dimensions))

Supporting Information

Full-color Waveguide-type Near-Eye Displays with Huygens' Metasurfaces

Weitao Song, Xinan Liang, Qijia Cheng, Parikshit Moitra, Xuewu Xu, Weijia Zhang, Xiaogang Shi, Yuanjin Zheng, Yongtian Wang, Ramón Paniagua-Domínguez*, Arseniy I. Kuznetsov**

Weitao Song, Weijia Zhang, Yongtian Wang
Beijing Engineering Research Center of Mixed Reality and Advanced Display, School of Optics and Photonics, Beijing Institute of Technology, 5 Zhongguancun South Street, Beijing, 100081, China
email: swt@bit.edu.cn
Xinan Liang, Parikshit Moitra, Xuewu Xu, Ramón Paniagua-Domínguez, Arseniy I. Kuznetsov
Institute of Materials Research and Engineering, A*STAR (Agency for Science, Technology and Research), 2 Fusionopolis Way, #08-03 Innovis, 138634, Singapore

email:Ramon_Paniagua@imre.a-star.edu.sg, and
Arseniy_Kuznetsov@imre.a-star.edu.sg
Qijia Cheng, Yuanjin Zheng
School of Electrical and Electronic Engineering, Nanyang Technological University, 50 Nanyang Avenue, 639798 Singapore

Xiaogang Shi
School of Integrated Circuits and Electronics, Beijing Institute of Technology, 5 Zhongguancun South Street, Beijing, 100081, China

Supporting Information

Figure S1. Illustration of grating patterns on the waveguides (units, mm).
Figure S2. Illustration of diffraction structures nano-printed on waveguide surfaces (units, nm).
Figure S3. Top-view (left) and cross-sectional (right) SEM images of the in-coupling grating for the green-blue channel waveguide.
Figure S4. Cross-sectional (left) and top-view (right) SEM images of the turning grating for the green-blue channel waveguide.
Figure S5. Cross-sectional (left) and top-view (right) SEM images of the outcoupling grating for the green-blue channel waveguide.
Figure S6. Photographs of (a) imprint mold and (b) uncut waveguide, showing two steps of the waveguide fabrication process.
Figure S7. Simulation results of beam distribution within the eye box for different fields of angles.
Figure S8. Diffraction efficiency of the waveguide as a function of wavelength.
Figure S9. The electric field profile (left) and magnetic field profile (right) in the nanodisk designed for the wavelength of 532nm at Huygens condition.
Figure S10. SEM image of a metasurface hologram fabricated with the staircase fabrication process.
Figure S11. System set-up for image projection using the designed metasurface holograms.
Figure S12. Possible near-eye display system set-up using the designed metasurface holograms.
Figure S13. Fabrication process of metasurface hologram.
Figure S14. Fabrication process of nanoimprint mold.
Table S1. Design parameters of TiO_2-based transmissive Huygens' metasurfaces.
Table S2. Simulated beam deflection efficiency at RGB wavelengths for the blazed gratings.

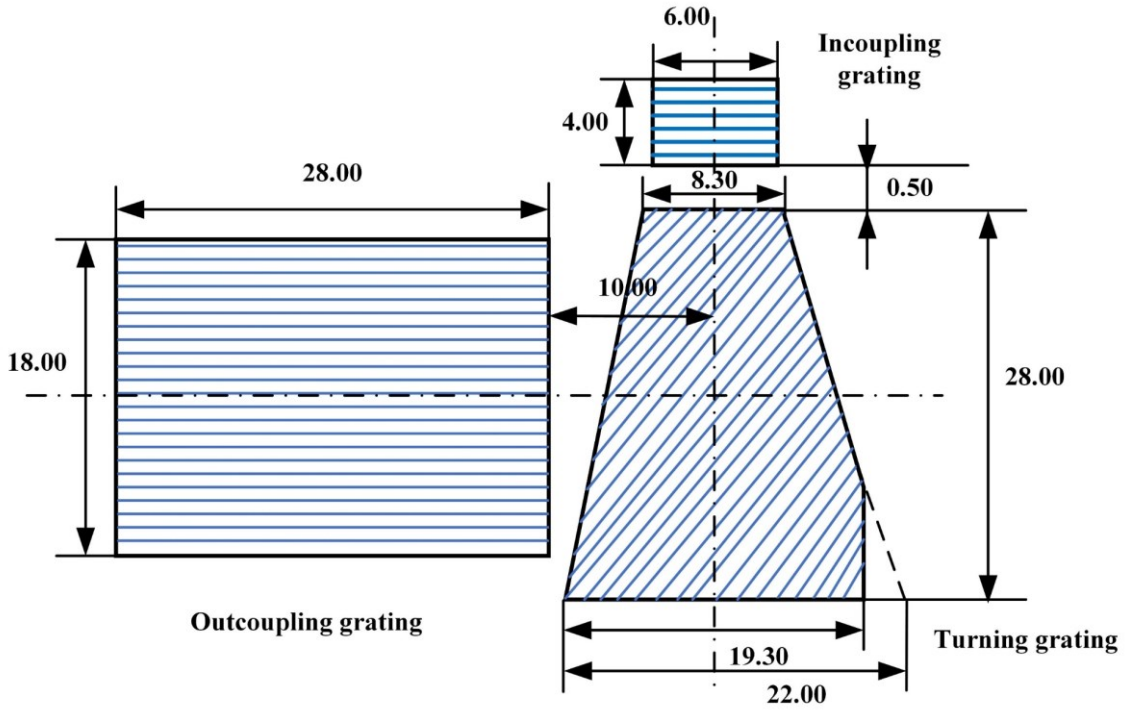

Figure S1. Illustration of grating patterns on the waveguides (units, mm). Two pieces of waveguide are bonded with each other, and they were designed for a green-blue channel and a red channel, respectively. Three grating structures are nano-printed on the waveguide, and their relative locations are shown in the figure.

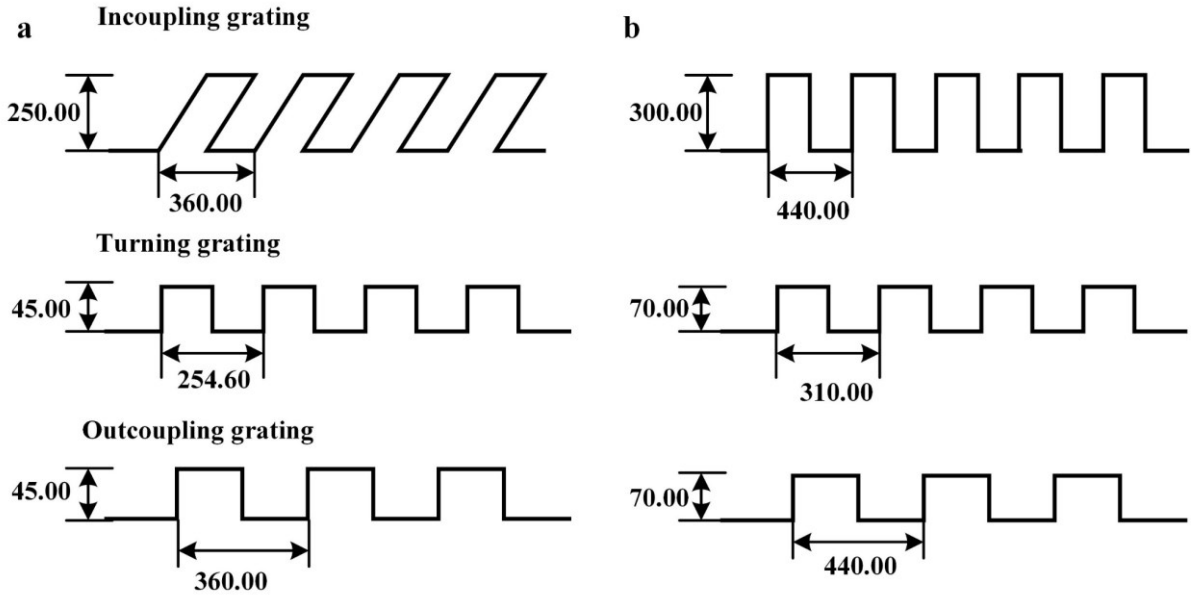

Figure S2. Illustration of diffraction structures nano-printed on waveguide surfaces (units, nm). (a) and (b) provide the diffraction structures for the green-blue channel and red channel, respectively.

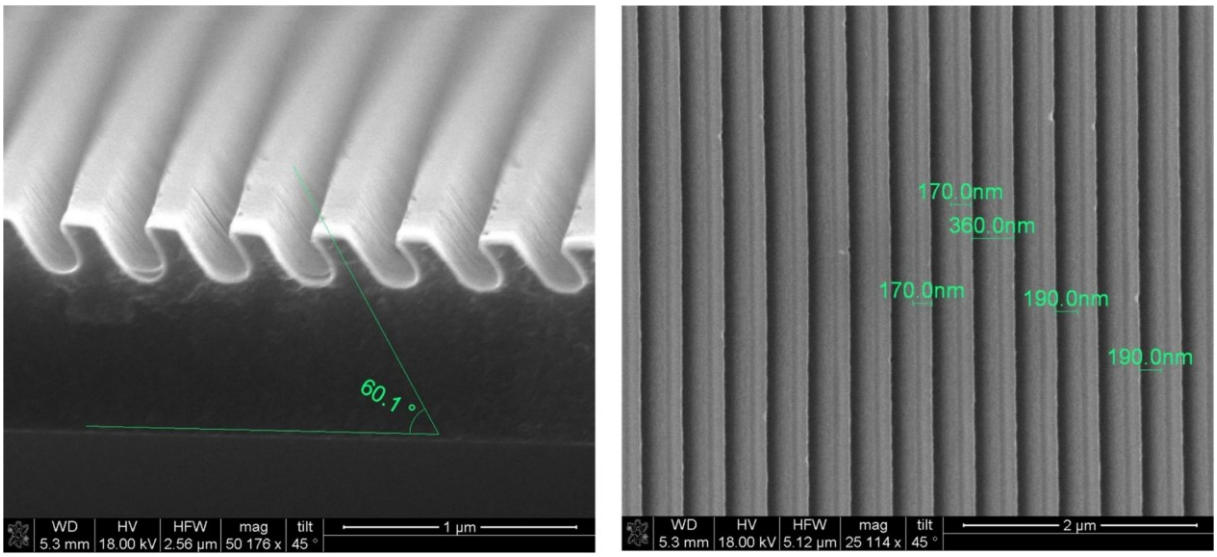

Figure S3. Top-view (left) and cross-sectional (right) SEM images of the in-coupling grating for the green-blue channel waveguide.

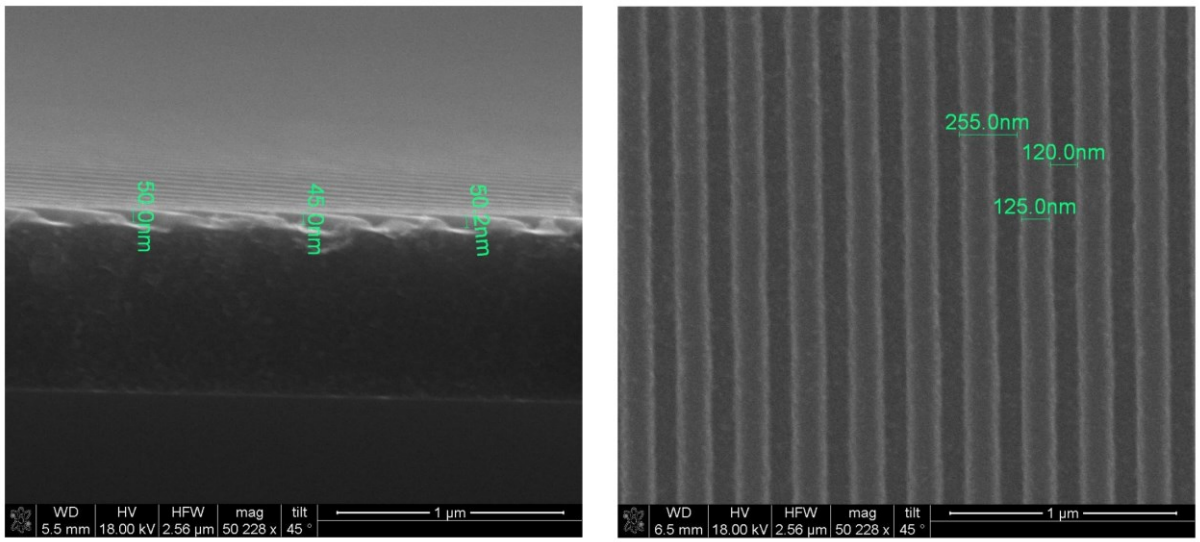

Figure S4. Cross-sectional (left) and top-view (right) SEM images of the turning grating for the green-blue channel waveguide.

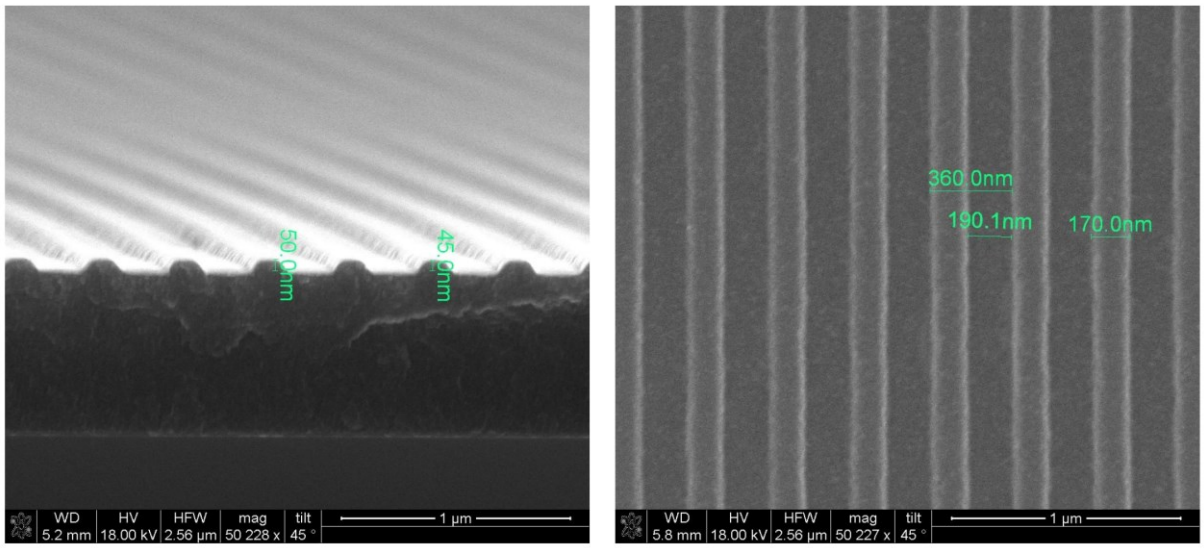

Figure S5. Cross-sectional (left) and top-view (right) SEM images of the outcoupling grating for the green-blue channel waveguide.

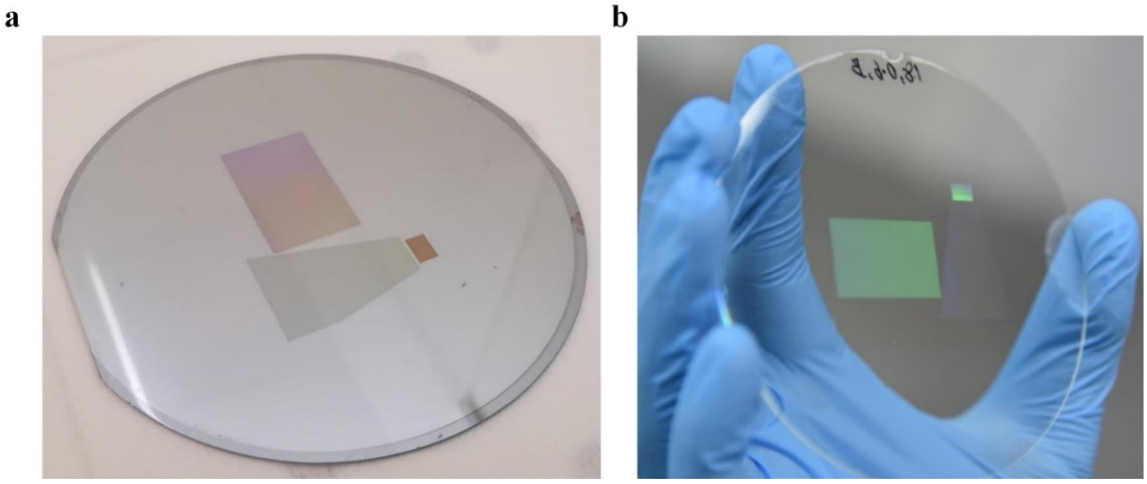

Figure S6. Photographs of (a) imprint mold and (b) uncut waveguide, showing two steps of the waveguide fabrication process.

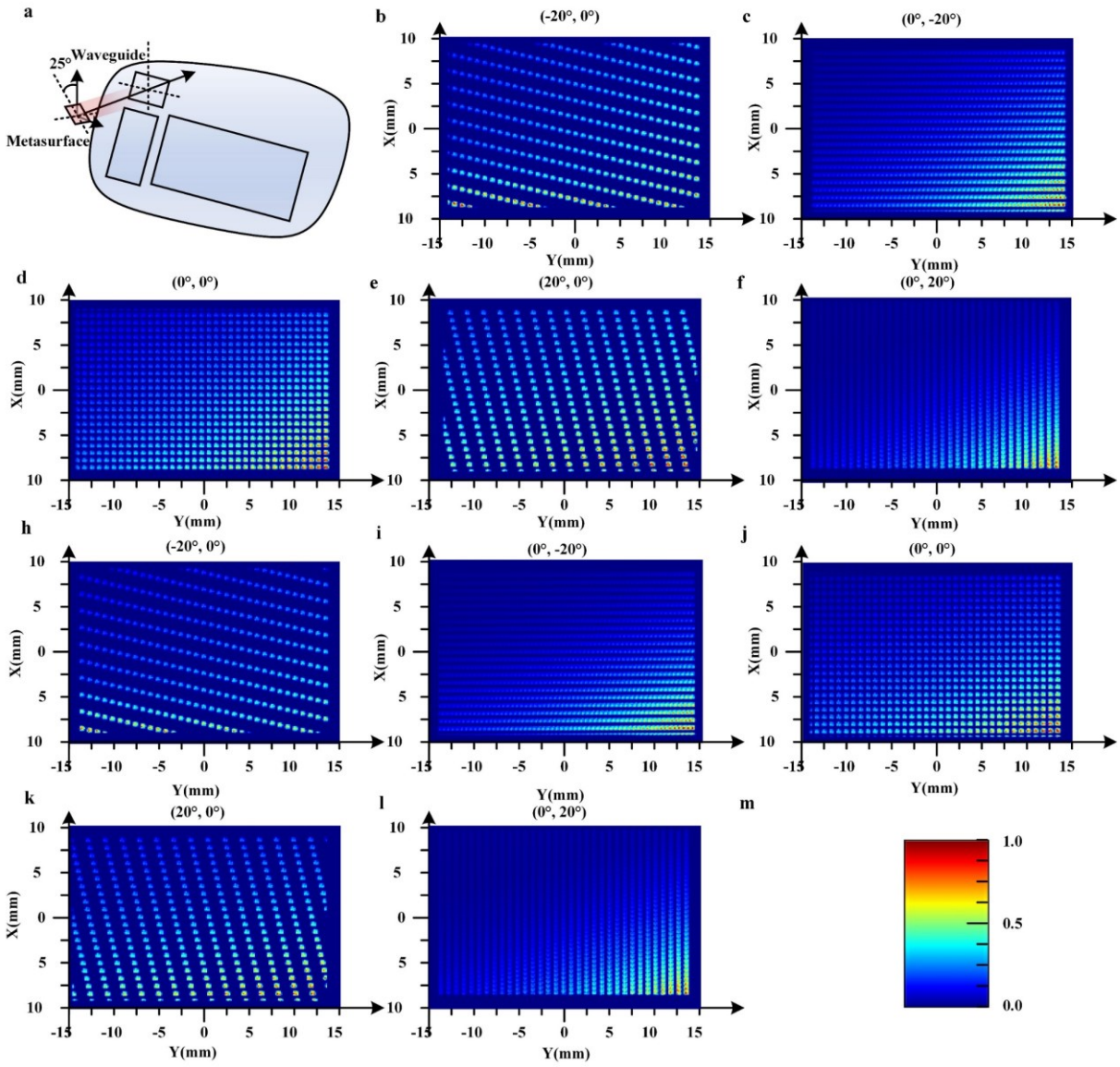

Figure S7. Simulation results of beam distribution within the eye box for different fields of angles. The performance of the diffractive waveguide (with three gratings) and the metasurface (0.5mm × 0.5mm) placed with a tilt of 25° to the waveguide normal are modeled in the simulation software. Five beams with different field of view ((-20°, 0°), (0°, -20°), (0°, 0°), (20°, 0°), and (0°, -20°)) are irradiated from the metasurface and coupled to the input grating. A receiver is placed at the position of the viewer's eye, 15mm away from the output grating. Two types of waveguides are analyzed individually. (b-f) and (h-l) show the simulation results of the waveguide performance for the red channel and green-blue channel respectively. All the data in each image have been normalized and pseudo-colored (see (m) for the color scale). The distance between adjunct beams emitting from the waveguide should be less than 2mm within the overall eye box and the field of view.

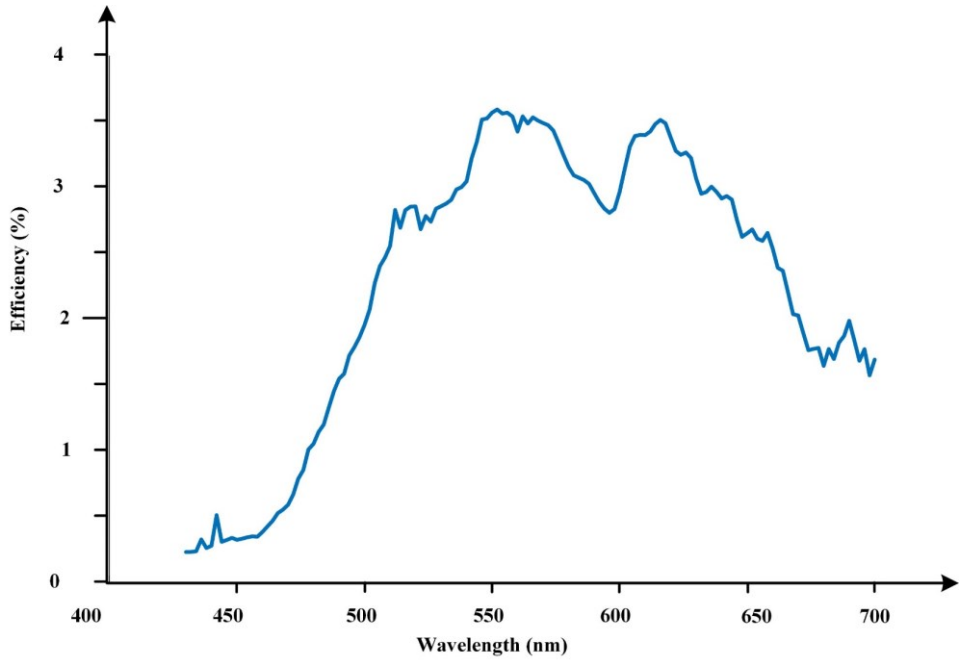

Figure S8. Diffraction efficiency of the waveguide as a function of wavelength.

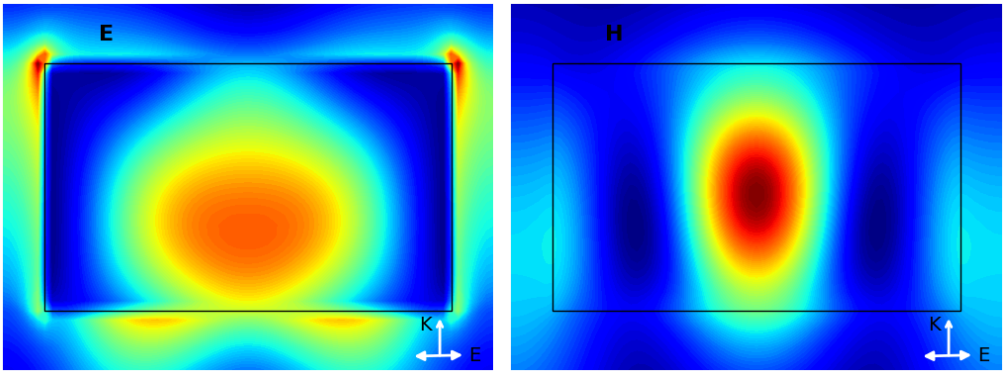

Figure S9. The electric field profile (left) and magnetic field profile (right) in the nanodisk are designed for the wavelength of 532nm at Huygens condition. The horizontal white arrow shows the incident light polarisation and the vertical arrow indicates the light propagation direction.

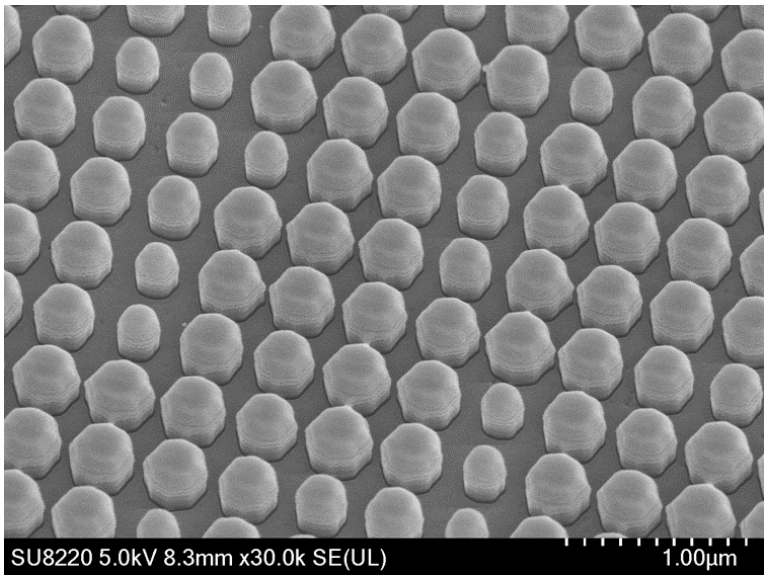

Figure S10. SEM image of a metasurface hologram fabricated with the staircase fabrication process.

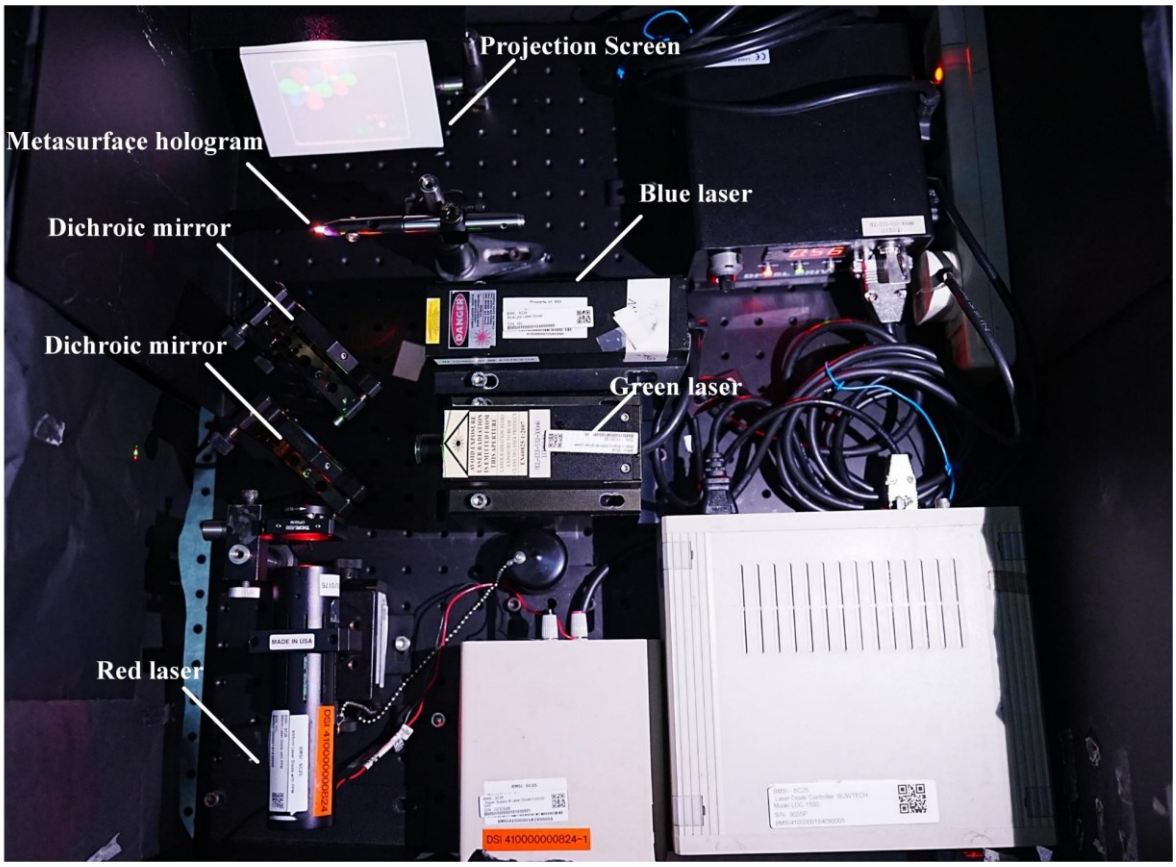

Figure S11. System set-up for image projection using the designed metasurface holograms.

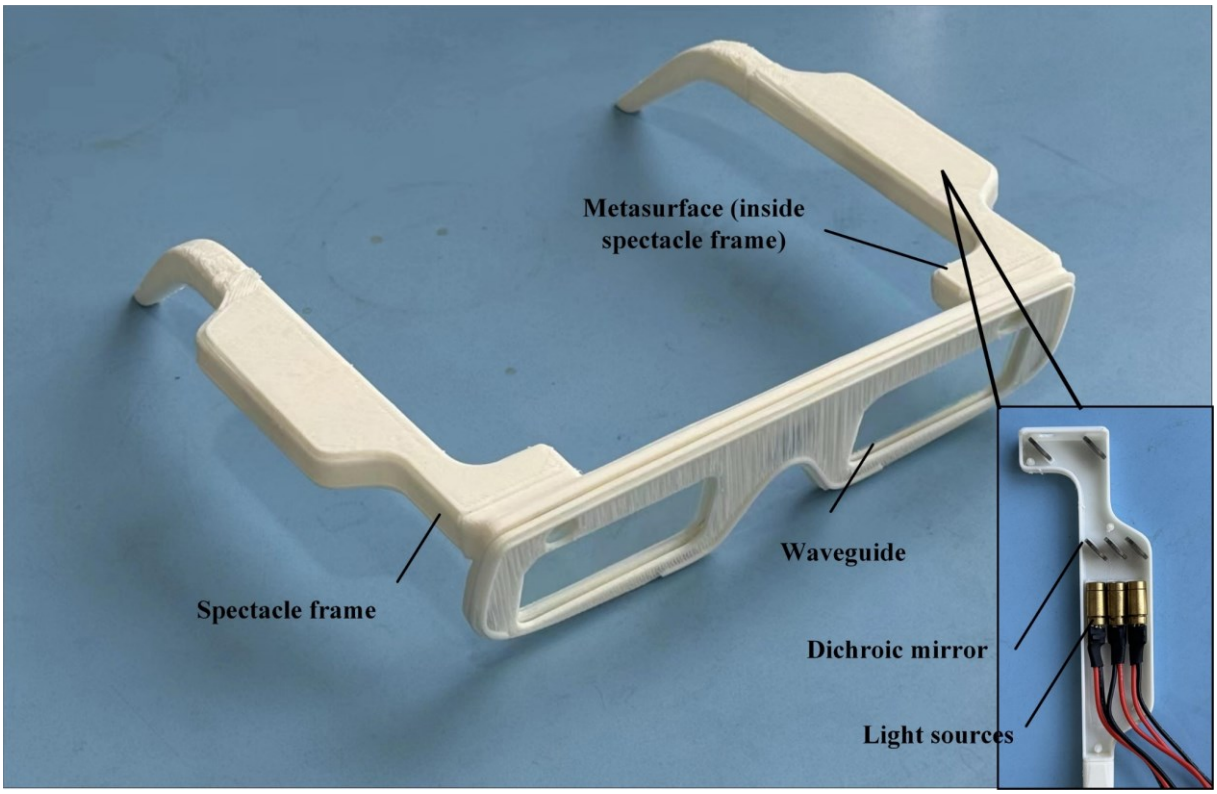

Figure S12. Possible near-eye display system set-up using the designed metasurface holograms.

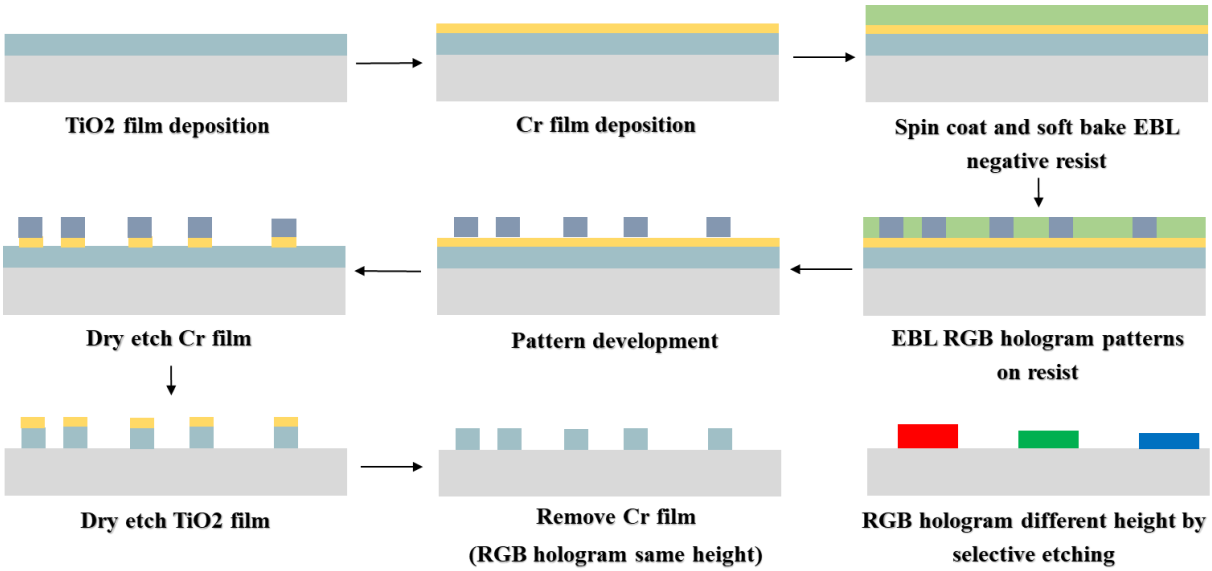

Figure S13. Fabrication process of metasurface hologram.

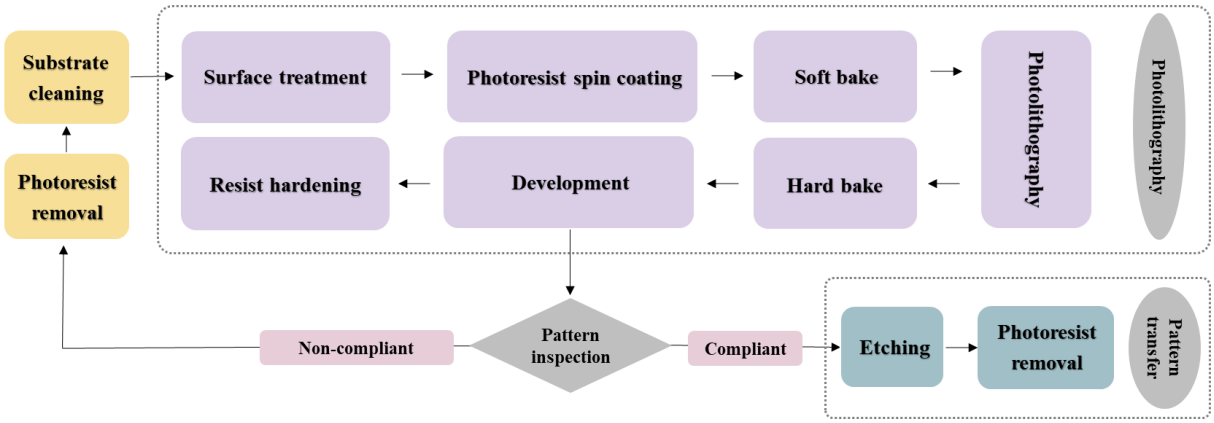

Figure S14. Fabrication process of nanoimprint mold.

Table S1 Design parameters of TiO_2-based transmissive Huygens' metasurfaces.

Wavelength (nm)	p (nm)	h (nm)	r (nm)
662 (Red)	420	172	185
532 (Green)	345	125	143
473 (Blue)	305	113	128

Table S2 Simulated beam deflection efficiency at RGB wavelengths for the blazed gratings.

Wavelength (nm)	0^{th} diffraction order transmission	$+1^{st}$ diffraction order transmission	-1^{st} diffraction order transmission	T (total transmission)
662 (Red)	16.5%	30.2%	0.37%	72.0%
532 (Green)	10.8%	36.0%	0.22%	72.3%
473 (Blue)	8.9%	32.5%	0.26%	73.4%